J Mater Sci (2007) 42:847–853
DOI 10.1007/s10853-006-0063-2

# Grain boundary engineering of 304 austenitic stainless steel by laser surface melting and annealing

**Sen Yang · Zhan Jie Wang · Hiroyuki Kokawa · Yutaka S. Sato**

Received: 19 September 2005 / Accepted: 20 March 2006 / Published online: 28 December 2006


**Abstract** In order to improve the intergranular corrosion resistance of 304 stainless steel, laser surface remelting experiments were conducted using a 2 kW continuous wave Nd: YAG laser. The grain boundary character distribution (GBCD) and microstructures of the materials were analyzed using EBSD, SEM and OM. The experimental results showed that combination of laser surface melting and annealing on 304 stainless steel resulted in a high frequency of twin boundaries and consequent discontinuity of random boundary network in the materials, which led to an improvement of resistance to intergranular corrosion. The maximum CSL density could reach 88.6% under optimal processing conditions: 1220 K and 28 h.

## Introduction

The 304 austenitic stainless steels are extensively used in nuclear, chemical and other industries owing to their relatively good corrosion and mechanical properties. But under some conditions such as improper thermal treatment, a sensitization problem, which is caused by chromium carbide ($Cr_{23}C_6$) precipitation at grain boundaries at 823–1173 K temperature ranges, renders this type of stainless steel susceptible to intergranular corrosion (IGC) attack. These attacks usually lead to the premature failure of components. To solve this problem, several remedies have been considered and applied, such as reduction carbon-content, addition of carbon stabilizing elements, rapidly cooling throughout the sensitization temperature range, and local desensitization [1–4]. However, there are some limitations for these methods in actual application.

Recent grain boundary structures studies have revealed that grain boundary phenomena strongly depend on the crystallographic nature and atomic structure of the grain boundary. Grain boundary structure dependence of intergranular precipitation and corrosion has been reported in nickel [5], nickel alloy [6], and austenite stainless steel [7]. Stickler et al. [8] reported that twin boundaries are not susceptible to carbide precipitation. Trillo et al. [9] found a remarkable resistance of coherent twin boundary to carbide precipitation. A great amount of researches showed that low Σ coincidence site lattice (CLS) boundaries (usually $\sum \leq 29$), especially $\Sigma 3^n$ ($n$ = 1, 2, 3) boundaries possess special chemical, mechanical, electronic, kinetic, and energy properties [10–17]. Of particular relevance to industrial materials, these special grain boundaries display a high resistance (and, in many cases, immunity) to sliding, cavitations, and fracture; corrosion and stress-corrosion cracking; sensitization; and solute segregation (equilibrium and nonequilibrium). Therefore, advancing in understanding the structures and properties of grain boundaries have resulted in the emergence of ''grain boundary design and control'' as a viable means of enhancing the bulk

S. Yang (✉)
Department of Materials Science and Engineering, Inner Mongolia University of Technology, Hohhot 010051, P.R. China
e-mail: yangsen@tsinghua.edu.cn

Z. J. Wang · H. Kokawa · Y. S. Sato
Department of Materials Processing, Graduate School of Engineering, Tohoku University, 6-6-02 Aramaki-aza-Aoba, Aoba-ku, Sendai 980-8579, Japan

properties of conventional polycrystalline materials, which has evolved the concept of grain boundary engineering (GBE) [6, 10]. Since then, the influence of structures and characters of grain boundary on the performances of polycrystalline materials has been extensively studied during the past three decades and still attracts a great of attention. The feasibility of GBE has been demonstrated mainly by thermomechanical treatment, which can be broadly divided into strain annealing and strain recrystallization processes [18]. Most recently, Shimada et al. [19] developed GBEed type 304 stainless steel by one-step strain annealing. An improvement of IGC resistance by this method was confirmed. TEM investigation showed that the depletion at a low-energy boundary segment introduced by twin emission into a random boundary was smaller than that of the original random boundary after sensitization. Up to now, the strain was mainly introduced by cold rolling. However, this method is only applicable for metal plate; it is not applicable for irregular shape. On the other hand, it generally needs a very long annealing time.

The previous researches showed that the low energy $\sum$ boundaries ($1 \le \sum \le 29$), especially $\sum 3^n$ boundaries, were correlated with the abnormal grain growth (AGG) occurred in polycrystalline [19]. Koo et al. [20–22] reported that there exists a critical strain for most of the metals. At the critical strain, some of the grain boundaries are distorted by extrinsic dislocation, which will induce rapid growth of some grains when the materials are annealed at a high temperature. If the initial grain size is very small, AGG will rapidly occur at high temperatures, even without any deformation, and the deformation effect will be less pronounced.

It is well known that laser surface melting (LSM) can remarkably fine the microstructures [23]. On the other hand, owing to the rapid cooling rate, there exists certain strain in the molten zone after solidification.

Therefore, the aim of this study is to combine LSM with annealing treatment to modify the grain boundary character distribution (GBCD), accordingly to improve the IGC resistance of 304 stainless steel.

## Experimental details

Commercial type 304-austenite stainless steel plate was used for this investigation. Table 1 lists the chemical composition. The rectangular specimens of $50 \times 8 \times 8$ mm were cut from alloy plate and solution annealed at 1323 K for 0.5 h followed by water quenched to eliminate any carbide precipitate formed during processing, which were named as base material (BM). In order to minimize the reflection for the laser beam and obtain a similar surface quality for each specimen, all the specimens were ground up to 600 grit SiC paper and cleaned in ethanol prior to LSM.

**Table 1** Chemical composition of 304-austenite stainless steel

| C | Si | Mn | P | S | Cr | Ni | Fe |
|---|---|---|---|---|---|---|---|
| 0.055 | 0.60 | 1.00 | 0.029 | 0.005 | 18.28 | 8.48 | Balance |

**Table 2** Laser processing parameters

| Scanning velocity, mm/s | Output power, W | Beam diameter, mm | Shielding gas, l/min | Overlapping ratio, % |
|---|---|---|---|---|
| 5–50 | 721–1415 | 3 | 15 | 30 |

LSM experiments were performed on a 2 kW Nd: YAG Laser (NEC 850) in CW mode. The normally incident laser beam was focused to a spot with diameter of 3 mm. During laser processing, a continuous flow of argon gas was blown to the melted zone to prevent heavy oxidation. The detailed laser processing parameters are list in Table 2. In order to obtain a larger melting area, overlapping technique was adopted, and the optimal overlapping ratio was 30%. Hereafter, specimen processed by LSM and annealed was termed as grain boundary engineered material (GBEM).

The laser surface melted specimens were annealed at 1200, 1220, and 1240 K for various times under air condition, respectively.

Specimens were cut along the laser-scanning track, and were prepared using the standard metallographic technique. In order to remove residual surface deformation and stress caused by mechanically grinding and polishing, specimens were electro-polished in a solution containing 10% perchloric acid in ethanol at a voltage of 30 V for 60 s. At last, the specimens were electro-etched in an oxalic acid solution at room temperature for 30 s to show grain boundaries. A Philips XL30 scanning electron microscopy equipped with a field emission gun (FEG) and a solid-state backscatter detector was used to obtain orientation image microscope (OIM), and the TSL$^{TM}$ analyzing software was used to analyze the GBCD. Grain boundaries were categorized in three group: LABs (low angle boundaries) with $\sum = 1$, CSLs with $1 < \sum \le 29$, and HABs (high angle boundaries) with $\sum > 29$, where the $\sum$ number is the reciprocal of the fraction of shared lattice sites from each grain at the

boundary. Brandon's criterion [24] was applied to determine the $\sum$ number for all boundaries.

In order to detect susceptibility to intergranular attack, a double loop electrochemical potentiokinetic reactivation (DL-EPR) test [25] was performed after being sensitized at 923 K for various time. The reactivation current ratio ($R_a$) was used to evaluate the susceptibility to IGC. The larger $R_a$ value is, the higher the susceptibility of the material to intergranular attack. Each sample was repeated at least two times in different solutions to ensure reproducibility. The surface morphologies of the samples after EPR test were observed by scanning electronic microscopy.

## Experimental results and discussions

### Microstructures and GBCD of BM

Figure 1(a) shows the typical microstructure of BM sensitized at 923 K for 20 h. It can be seen that nearly continuous Cr-rich carbides were precipitated at most of the grain boundaries, even though at the special boundaries due to the severe sensitization. Figure 1(b) shows the corresponding GBCD of the BM. Random and CSL boundaries are indicated by thick black line and thin gray line, respectively. In the BM, the fraction of CSL boundaries was only 57.6%, which was composed of 34.8% Σ3, 4.0% Σ9 and 1.0% Σ27, and the random grain boundaries (RGBs) showed a continuous network. The fact that the Cr-rich carbides easily precipitate at the RGBs led to the formation of the continuous Cr-rich carbides, which meant that BM was susceptibility to intergranular attack. Therefore, these are boundaries with the potential for a continuous path for crack propagation.

### Microstructure characteristics of LSM

Figure 2 shows typical macro-scale morphology of the molten pool from the longitudinal cross-section. It can be observed that there existed three distinctive zones, namely, laser-melted zone (LMZ), heat-affected zone (HAZ), and the substrate. Figure 3(a) shows the microstructure of HAZ. In the HAZ, no carbides were observed at the grain boundaries, which meant that desensitization occurred in this zone. On the one hand, heat conducted from the melted zone during the laser-melting process made the pre-existed Cr-rich carbides completely dissolve. On the other hand, AGG occurred under the effects of heat input, which led to the change of GBCD. Figure 3(b) shows the GBCD of HAZ. Table 3 lists the fraction of the special CSL boundaries in LMZ and HAZ after laser surface

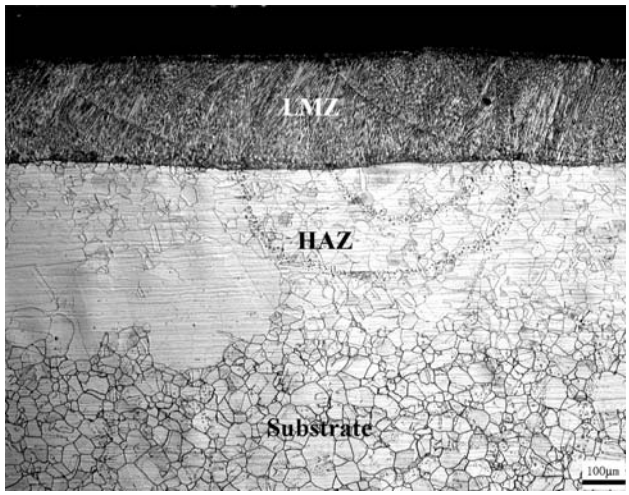


**Fig. 2** Macrograph of the molten pool from the longitudinal cross-section

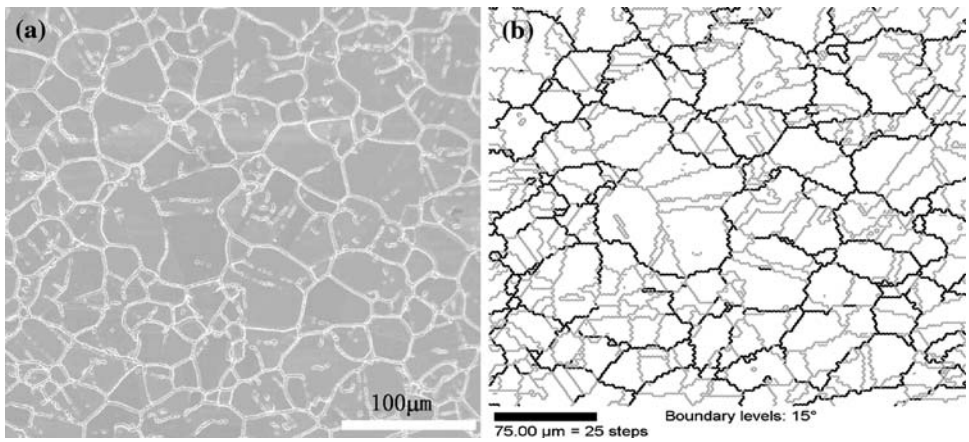


**Fig. 1** Microstructures of BM sensitized at 923 K for 20 h (**a**) and its corresponding GBCD (**b**). Random grain boundaries and low $\sum$ ones indicated by black line and gray line in (**b**), respectively

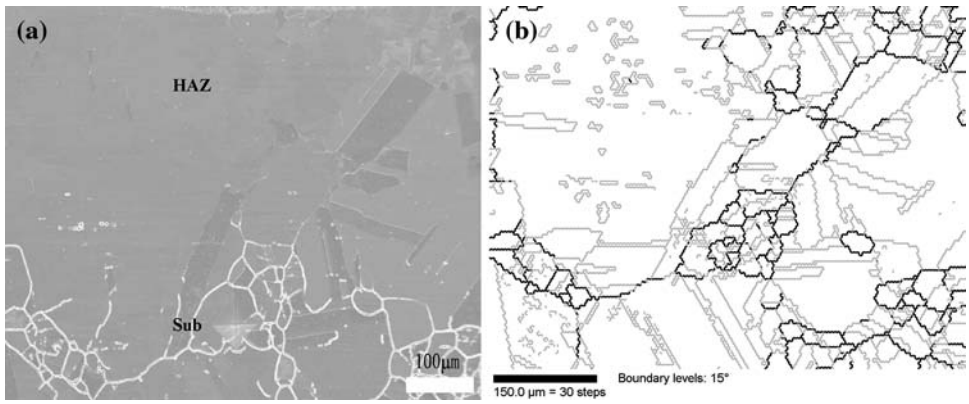


**Fig. 3** Microstructure of HAZ (**a**) and its corresponding GBCD (**b**). Random grain boundaries and low $\sum$ ones indicated by black line and gray line in (**b**), respectively

**Table 3** The fraction of the special CSL boundaries after LSM, %

| Position | Σ1 | Σ3 | Σ9 | Σ27 | Σ(1–29) |
|---|---|---|---|---|---|
| BM | 12.0 | 34.8 | 4.0 | 1.0 | 57.6 |
| HAZ | 12.1 | 55.3 | 4.0 | 0.8 | 74.9 |
| LMZ | 46.0 | 32.7 | 3.3 | 0.4 | 84.1 |

melting (LSM). It can be seen that a large amount of twin boundaries ($\sum 3$) were formed in the HAZ after LSM. The fraction of CSL boundaries was 74.9%, which was also higher than that of BM, 57.6%.

Figure 4(a) shows the microstructures of the LMZ. As observed in this figure, the microstructures of LMZ were remarkably fined, and the average primary cellular/dendritic spacing was only about 5 μm. The microstructure of LMZ was mostly composed of austenite with delta phase in the intercellular regions, which was consistent with the other investigations [1]. During laser surface melting processing, the pre-existed Cr-rich carbides had been completely dissolved due to the high heat flux density of the laser beam and will not re-precipitate in the following solidification processing due to the rapid solidification rate. Another important reason was that laser surface melting made the GBCD change obviously. Figure 4(b) shows the GBCD of the LMZ. Due to that there existed an ultra-high temperature gradient in the molten pool (generally $>10^6$K/m), microstructures directionally grew from the bottom to the top surface of the molten pool along <100> orientation, which led to that a large amount of LABs ($\sum 1$), 46%, and the amount of low-Σ CSL boundaries also increased and reached 84.1%. But these boundaries easily become a continuous path for intergranular corrosion crack propagation from the outmost surface into interior and make the materials much more susceptible to IGC. However, this kind of structure was metastable, and both of the microstructure and GBCD were changed in the following annealing treatment.

## GBCD after annealing treatment

Figure 5(a) shows the typical microstructure of the specimens annealed at 1200 K for 30 h. It can be seen that there existed no longer obvious boundary between LMZ and HAZ, and the average grain size became larger. Table 4 lists the average special CSL boundary percentages under various processing conditions. It can be found that the grain boundaries were primarily composed of low $\sum$ boundaries, especially $\sum 3^n$ boundaries. Accompanying by the formation of high frequency $\sum 3^n$ boundaries, the continuous RGB network was extremely dispersed by introduction of low

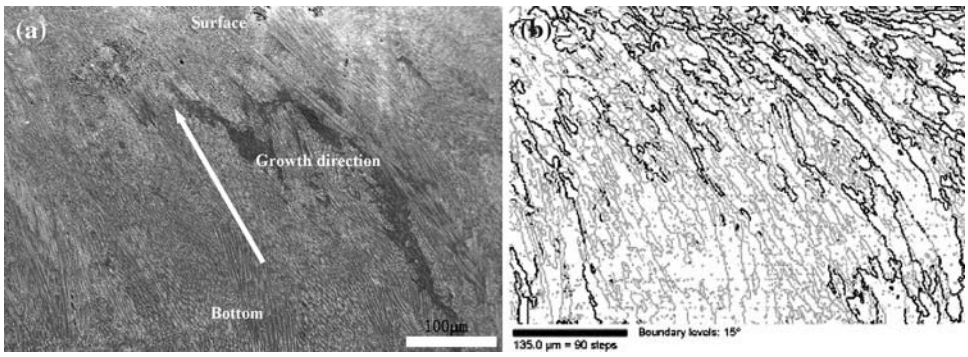


**Fig. 4** (**a**) Microstructure of the LMZ; (**b**) GBCD. Random grin boundaries and low $\sum$ ones indicated by black line and gray line in (**b**), respectively

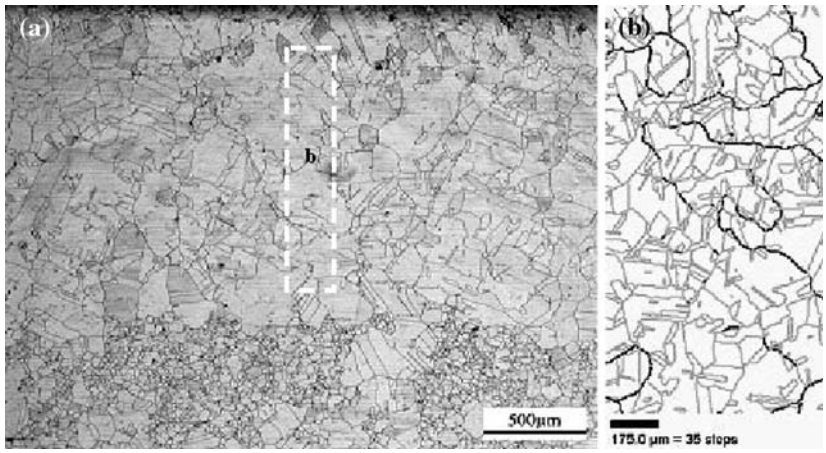


**Fig. 5** (**a**) Microstructure of specimen annealed at 1200 K for 30 h; (**b**) GBCD of zone b in (**a**). Random grain boundaries and low $\sum$ ones indicated by black line and gray line in (**b**), respectively

**Table 4** The fraction of the special CSL boundaries under various processing conditions, %

| Annealing condition | Σ1 | Σ3 | Σ9 | Σ27 | Σ(1–29) |
|---|---|---|---|---|---|
| 1200 K/48 h | 4.1 | 67.6 | 9.0 | 3.4 | 86.5 |
| 1220 K/28 h | 7.8 | 66.4 | 8.5 | 4.1 | 88.4 |
| 1240 K/48 h | 8.0 | 62.1 | 7.3 | 4.4 | 83.8 |

energy segments on migration random boundaries during twin emission and boundary–boundary reactions in the grain growth, see Fig. 5(b). Figure 6 shows the relationship between the fractions of low $\sum(1 \le \sum \le 29)$ boundaries and annealing time under various annealing temperature conditions. With increase of the annealing time, the fraction of the low $\sum$ boundaries increased. It took about 48 h and 28 h to attain the maximum frequency of the $\sum$ boundaries when the annealing temperature was 1200 K and 1220 K, respectively. But when the specimens were annealed at 1240 K for the same time, the frequency of the low $\sum$ boundaries was obviously less than those obtained at 1200 K and 1220 K. It can be found that the frequency of the $\sum$ boundaries was temperature dependent, and the reason may be attributed to the transition of the type of grain boundary plane during annealing treatment. It was pointed out that AGG occurred when all or some of the grain boundaries were faceted, and the fraction of the faceted grain boundaries decreased while the fraction of the smoothly curved increased with increase of the annealing temperature [20–22]. At high temperatures, grain boundaries became defaceted, with smoothly curved shapes, and then atoms could readily move across the grain boundaries, causing continuous grain boundary motion and showing normal grain growth. It is noted that there was no apparent effects of the laser processing parameters on the final frequency of the $\sum$ boundaries. It is well known that the microstructures and the strain level in laser processed zone greatly depend on processing parameters, such as scanning velocity and laser output power. In our experiments, a high output power generally corresponded to a high scanning velocity, vice versa. Under this condition, the scale of the microstructure and the strain level in the processed zone should be on the same order of magnitude. Therefore, there were no apparent effects of the laser processing parameters on the final annealing structure characteristics and GBCD. With respect to effects of laser processing parameters, it will be investigated detailed in another following paper.

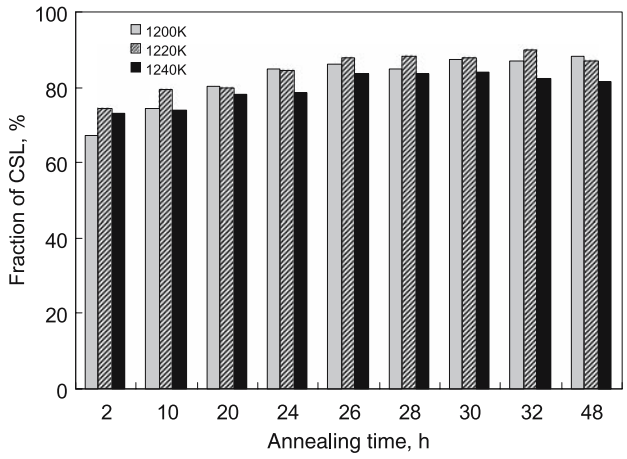


**Fig. 6** Relationship between the fraction of low Σ boundaries and annealing temperature and time

It is well known that grain growth depends on the strain level in materials. Generally speaking, a large strain tends to promote recrystallization, which will result in corrosive random boundaries and also CSL boundaries while a small strain accelerates grain

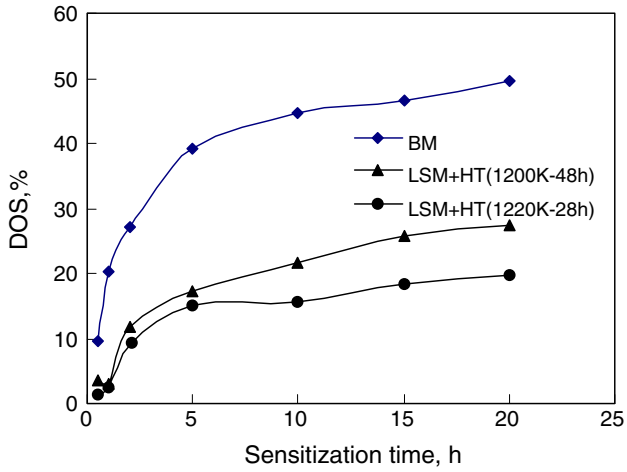


**Fig. 7** Relationship of the reactive current ratio and sensitization time

boundary migration without new grain generation. During thermomechanical treatment, a migration grain boundary inevitably interacts with lattice dislocations and other grain boundaries during grain growth. As the absorption rate of lattice dislocation by a low energy boundary [26] is much lower than that of a random boundary, a low energy boundary cannot move a long distance and the migration will never occur before completion of the absorption [27]. At the same time, the reactions possibly change the grain boundary structures to lower energy ones at high temperatures [28]. Therefore, a low energy boundary tends not to move, while a high-energy boundary can migrate widely and has a greatly opportunity for interaction with other boundaries or twin emissions so as to produce new low energy segments.

## IGC resistance

Figure 7 shows the relationship between the ratio of reactive current and sensitization time under various processing conditions. By combining LSM and annealing treatment, the ratios of the reactive current were much smaller than those of the BM, which meant that susceptibility to intergranular attack of BM has been remarkably reduced. This reduction could be confirmed by observing the surface morphologies of the specimens after EPR tests. Figure 8(a) shows the surface morphology of the BM after EPR test. Owing to there existed continuous RGBs in the BM; a severe and deep attack was clearly observed after EPR test. In contrast, GBEed specimens only suffered from slight grain boundary attacks owing to introduction of a large amount of low energy CSL boundaries, especially $\Sigma 3^n$ boundaries, as shown in Fig. 8(b), which further confirmed that the resistance to IGC was improved through the above-mentioned thermomechanical processing. Fullman et al. [29] pointed out that a low energy structure is stable and resistant to interaction with defects. Also, Kokawa's experiment [30] clearly showed the chromium depletion at a low-energy boundary segment introduced by twin emission into a random boundary was smaller than that of the original random boundary after sensitization. As above mentioned, the formation of annealing twin generally reduces the grain boundary energy during grain growth and the grain boundary energy of the part where twin emission occurs is likely lower than that of the initial random boundary, therefore, formation of a twin can introduce a low energy segment into the random high angle grain boundary and can sometimes lead to low $\Sigma$ CSL structures. Active twin events and reactions increase the frequency of CSL boundaries and also frequently produce low energy segments in high-energy boundaries locally annealing treatment. Well-distributed low energy segments in the grain network create a discontinuous chain of chromium depletion, which arrest the propagation of intergranular corrosion from the surface into the interior of the materials.

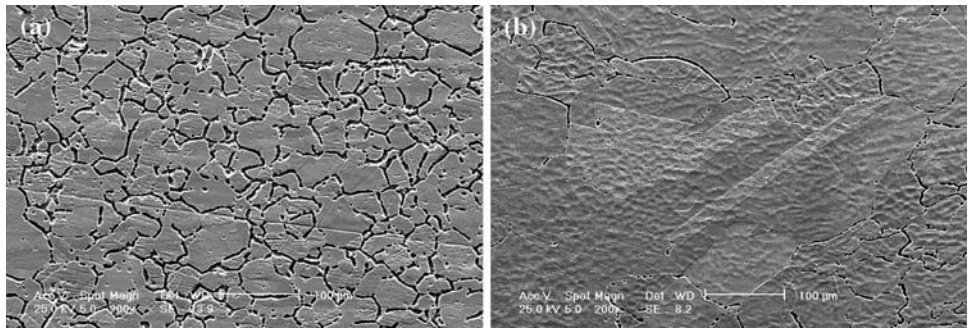


**Fig. 8** Surface morphology of specimens after EPR test (**a**) BM, (**b**) GBEM

## Conclusions

An optimized grain boundary character distribution with a high frequency of low Σ CSL boundaries, especially $\Sigma 3^n$ boundaries could be achieved by combining LSM with annealing treatment. The introduction of the high frequent low-energy grain boundaries during thermomechanical processing disrupted the continuous random grain boundaries network.

The optimal processing parameters were 1220 K and 28 h, and no obvious effects of the laser processing parameters on the final microstructures and grain boundary character distribution were observed.

An excellent resistance to IGC of 304 stainless steel was achieved by combining LSM with annealing treatment.

**Acknowledgements** One of the authors (S. Yang) is grateful to Japan Society for the Promotion of Science for offering a JSPS fellowship. The authors would like to express their gratitude to Dr. Y. S. Kang, Mr. A. Honda and Mr. Isago for their technical support. The partial support of this work Program for New Century Excellent Talents in University from Ministry of Education of China and Science Foundation of IMUT are also acknowledged.

## References

1. Akgun OV, Inal OT (1992) J Mater Sci 27:2147
2. Conde A, Colaco R, Vilar R, Damborenea Jde (2000) Mater Design 21:441
3. Anthony TR, Cline HE (1978) J App Phys 49:1248
4. Akgun OV, Inal OT (1995) J Mater Sci 30:6097
5. Alexandreanu B, Was GS (2006) Script Mater 54:1047
6. Lin P, Palumbo G, Erb U, Aust KT (1995) Script Metall Mater 33:1387
7. Kurban M, Erb U, Aust KT (2006) Script Mater 54:1053
8. Stickler R, Vinckier (1963) Mem Sci Rew Metall 60:489
9. Trillo EA, Murr LE (1999) Acta Mater 47:225
10. Watanabe T (1984) Res Mechanica 11:47
11. Kokawa H, Watanabe T, Karashima S (1981) Philos Mag A 44:1239
12. Watanabe T, Tsurekawa S (1999) Acta Mater 47:4171
13. Lehockey EM, Palumbo G, Lin P (1998) Meatll Trans A 29:3069
14. Hirata T, Tanabe S, Kohzu M, Higashi K (2003) Script Mater 49:891
15. Aust KT (1994) Can Metall Quart 33:265
16. Yamamura S, Tsurekawa S, Watanabe T (2003) Mater Trans 44:1494
17. Krupp U, Kane WM, Liu XY, Dueber O, Laird C, McMahon CJ (2003) Mater Sci Eng A 349:213
18. Randle V (1999) Acta Mater 47:4187
19. Shimada M, Kokawa H, Wang ZJ, Sato YS, Karibe I (2002) Acta Mater 50:2331
20. Koo JB, Yoon DY (2001) Metall Mater Trans A 32:469
21. Koo JB, Yoon DY, Henry MF (2002) Metal Trans A 33:3803
22. Lee SB, Hwang NM, Yoon DY, Henry MF (2000) Metall Trans A 31:985
23. Yang S, Huang WD, Lin X, Su YP, Zhou YH (2000) Script Mater 42:543
24. Brandon DG (1966) Acta Metall 14:1479
25. Majidi AP, Streicher MA (1984) Corrosion 40:584
26. Kokawa H, Watanabe T, Karashima S (1983) J Mater Sci 18:1183
27. Pumphrey OH, Gleiter H (1974) Philos Mag 30:593
28. Kokawa H, Watanabe T, Karashima S (1983) Scripta Metall 17:1155
29. Fullman RL, Fisher JC (1951) J Appl Phys 22:1350
30. Bi HY, Kokawa H, Wang ZJ, Shimada M, Sato YS (2003) Script Mater 49:219